Electron nuclear interactions in spin-3/2 color centers in silicon carbide: A high-field pulse EPR and ENDOR study

Victor A. Soltamov,[1] Boris V. Yavkin,[2] Georgy V. Mamin,[2] Sergei B. Orlinskii,[2] Ilia D. Breev,[1] Anna P. Bundakova,[1] Roman A. Babunts,[1] Andrey N. Anisimov,[1] and Pavel G. Baranov[1]

[1]*Ioffe Institute, Politekhnicheskaya 26, 194021, St. Petersburg, Russia*

[2]*Federal Center of Shared Facilities of Kazan State University, 420008 Kazan, Russia*

(Received 17 July 2020; revised 3 September 2021; accepted 8 September 2021; published 30 September 2021)

High-frequency pulsed electron paramagnetic resonance (EPR) and electron nuclear double resonance (ENDOR) were used to determine electron nuclear interactions on remote ligand shells of silicon and carbon in spin-3/2 color centers with an optically induced high-temperature spin alignment in hexagonal 4*H*-, 6*H*-, and rhombic 15*R*-silicon carbide (SiC) polytypes. The EPR and ENDOR experimental data relate unambiguously to spin-3/2 centers in which the optically induced alignment of the spin-level populations occurs. The identification is based on resolved ligand hyperfine interactions with carbon and silicon nearest, next-nearest, and the more distant neighbors and on the determination of the unpaired electron spin densities. The hyperfine interactions with ^{29}Si and ^{13}C nuclei are unambiguously separated due to the selective population of the fine-structure levels with certain values of M_S. The signs of these interactions and, as a result, the signs of oscillating spin density at ^{29}Si and ^{13}C nuclei, are determined. On the basis of the EPR and optically induced ENDOR measurements, signs of the fine-structure splitting for all the centers were demonstrated, which made it possible to establish the character of optically induced spin alignment, including the inverse populations of the spin levels for these centers. The values of hyperfine interaction with ^{29}Si and ^{13}C nuclei, including those remote from the localization of the spin-3/2 center, are tabulated, which can be used by a number of algorithms in quantum information processing as long-term memory.

DOI: 10.1103/PhysRevB.104.125205

I. INTRODUCTION

Silicon carbide (SiC) is a well-developed wide band-gap semiconducting material widely used for applications in high-frequency, high-temperature, high-power, and radiation-resistant electronic devices. The primary defects in SiC are vacancies, interstitials, and antisites. In contrast to silicon [1] the primary defects in SiC are stable even much more above room temperature, and can be found at various sites in the different polytypes that arise from differences in the stacking sequence of the Si-C bilayers. The cubic 3*C*-SiC, hexagonal 4*H*-, 6*H*-SiC, and rhombic 15*R*-SiC polytypes are the most common and most appropriate for applications. In 3*C*-SiC only one cubic sublattice site is present. In 4*H*-SiC two nonequivalent crystallographic positions exist, one hexagonal and one quasicubic site, called h and k, respectively. In 6*H*-SiC three nonequivalent positions are formed, one hexagonal and two quasicubic ones, called h, k_1, and k_2. In 15*R*-SiC five nonequivalent positions are formed, two hexagonal and three quasicubic ones, called h_1, h_2, k_1, k_2, and k_3. The nearest neighbors (the first shell) are nearly tetrahedrally oriented for all sites, but the second shells are different for the hexagonal and quasicubic sites. The quasicubic sites differ in the third shell of neighbors.

Optically active defects, also referred to as atomic-scale color centers in bulk and nanocrystalline SiC are promising for quantum information processing, photonics, and sensing at ambient conditions. Their spin state can be initialized, manipulated, and read out by means of optically detected magnetic resonance (ODMR). Until recently, practical applications of semiconductors have been associated with using defect ensembles. The unique quantum properties of the negatively charged nitrogen-vacancy (NV^-) center in diamond [2] have motivated efforts to find defects with similar properties in SiC, which can extend the functionality of spin color centers not available to the diamond. Such systems are the most prominent objects for applications in new generation of supersensitive magnetometers, biosensors, single-photon sources [2–8]. The diamond NV defect is in many ways the ideal qubit, but it is currently quite difficult to fabricate devices from diamond. It remains difficult to gate these defects electrically. A search to find defects with even more potential ("better than excellent") had been launched [9–14], manifested itself by the great progress in understanding and exploiting color centers in SiC. Unique chemical, electrical, optical, and mechanical properties make this material very attractive for applications under extreme conditions and can open up a whole new world of scientific applications in spintronics.

A convincing point with SiC is that the stable spinless nuclear isotopes guarantee long dephasing times. Unusual polarization properties of various vacancy-related centers in SiC (labeled as P3, P5, P6, and P7) were observed by means of electron paramagnetic resonance (EPR) under optical excitation and reported for the first time in the works of Refs. [15,16], later in Refs. [9,10,17–22]. One of the main questions was to establish whether the observed EPR spectra

TABLE I. Zero-phonon line energy/wavelength at 10 K; values of zero-field splitting Δ ($\Delta = 2|D|$) and g factor of the each center at room temperature for family of V1, V2, V3, and V4 spin-3/2 centers in the 4*H*-SiC, 6*H*-SiC, and 15*R*-SiC. Spin sublevels possessing optically induced predominant population observed at room temperature in zero magnetic field (optically induced spin alignment) are shown in the last row.

Polytype	4*H*-SiC		6*H*-SiC			15*R*-SiC		
Zero-phonon line	V1	V2	V1	V2	V3	V2	V3	V4
E, eV/λ, nm	1.438/862	1.352/917	1.433/865	1.397/887	1.368/906	1.399/886.5	1.372/904	1.352/917
ΔMHz/10^{-4} cm^{-1}	7.1/2.4 [19]	66/22	27/9	128/42.7	27/9	139.2/46.4	11.6/3.87	50.2/16.7
D MHz/10^{-4} cm^{-1}	39/13	33/11	−13.5/−4.5	64/21.35	−13.5/−4/5	69.6/23.2	−5.8/−1.94	25.1/8.35
g factor	2.0032	2.0032	2.0032	2.0032	2.0032	2.005(1)	2.005(3)	2.005(3)
Zero field at room temperature optically induced level alignment		±1/2	±1/2 inverse population	±3/2 inverse population	±1/2 inverse population	±3/2 inverse population	±1/2 inverse population	±1/2

belong to the ground or to the excited state. EPR experiments performed at high frequency and at very low temperatures in darkness excluded the possibility of thermal or optically excited states and as a result it was proved that the EPR spectra of P3, P5, P6, and P7 defects belong to the ground state for all the defects [9,10,22]. It has been shown that there are at least two families of color centers in SiC, which have the property of optical alignment of the spin levels and allows a spin manipulation at ambient conditions. (i) Family of spin-triplet ($S = 1$) color centers, widely represented in SiC by silicon-carbon divacancies (covalently bonded closest pair of silicon and carbon vacancies). The symmetry of these centers is due to the direction of connection between the silicon and the carbon; zero-field splittings for these centers as in the case of the NV^- center in diamond are in the gigahertz range. (ii) Family of silicon-vacancy related centers having quadruplet ground and excited states ($S = 3/2$). Recent experiments demonstrated [9,10,13,20,22–49] that several highly controllable defects exist in SiC, and some of them can be spin manipulated at room temperature or even higher.

Spin-3/2 silicon-vacancy related centers in SiC are demonstrated to be a promising quantum system for single-spin and single-photon spectroscopy. It is assumed that these centers are designated as the corresponding zero-phonon lines: V1, V2, V3, and V4. Their basic spectroscopic parameters, determined for the main SiC polytypes, namely 4*H*, 6*H*, and 15*R*, are presented in Table I.

Zero-field ODMR shows the possibility to manipulate of the ground-state spin population by applying radio-frequency (rf) field which is compatible with NMR techniques and using the infrared optical pumping which is compatible with optical fibers and band of transparency of living matter. These altogether make spin-3/2 V_{Si}-related defects in SiC very favorable candidate for spintronics, quantum information processing, magnetometry, and thermometry.

Recently, the existence of NV^- centers in SiC with $S = 1$ has been demonstrated in Refs. [50–53] and can be expected to hold similar promising properties as the NV^- centers in diamond and divacancies in SiC. The N_C-V_{Si} centers have been identified in different (3*C*, 4*H*, 6*H*) polytypes of SiC. In the negative charge state, they are spin $S = 1$ centers with optical properties shifted to the near-IR region (around 1200-nm wavelength).

At the initial stage of the radiation defect study, EPR spectra of silicon vacancies in the negatively charged state (V_{Si}^-) were found [49]. An important circumstance was that the parameters of the spin Hamiltonian of these vacancies depended little on the polytype of silicon carbide (cubic, hexagonal, or rhombic) and the vacancy position (cubic or hexagonal) in the crystal lattice. It should be emphasized that the zero field splitting for these vacancies, which have an electron spin $S = 3/2$, is practically zero. Careful studies of g factors by the high-frequency EPR method [22] discovered an extremely small difference in g factors for hexagonal and cubic vacancy positions in 4*H*-SiC which clearly demonstrated the presence of two positions for the V_{Si}^-.

The purpose of this work is to determine hyperfine (HF) interactions with surrounding silicon (^{29}Si) and carbon (^{13}C) atoms for silicon-vacancy related $S = 3/2$ centers in which the optically induced alignment of the spin-level populations occurs, and thereby find the distribution of the spin density at these atoms. It is important to emphasize that in a number of algorithms on the application of spin centers in SiC in quantum processing, the possibility of using nuclear spins of ^{29}Si and ^{13}C as a long-term memory is considered. For these purposes, naturally, information is needed on hyperfine interactions with these nuclei, including remote nuclei from the site of the localization of the spin center. This information was obtained using the electron nuclear double-resonance (ENDOR) research in this paper.

II. EXPERIMENT

4*H*-SiC, 6*H*-SiC, and 15*R*-SiC crystals were grown by the sublimation technique [54] in vacuum at temperatures between 1700 and 1750 °C and with concentrations of uncompensated nitrogen (N) donors in the range 10^{16}–10^{17} cm^{-3}. These samples were irradiated with fast neutrons to a dose up to 10^{18} cm^{-2} or electrons with the energy of 1–2 MeV with doses ranging from 10^{15} to 10^{16} cm^{-2}. No annealing treatment was applied. Typical concentration of the V_{Si}-related color centers was of $\sim 10^{15}$ cm^{-3}. The epitaxial SiC layers as well as samples of high crystalline quality grown by the Lely method were also investigated. In some ENDOR experiments ^{13}C isotope-enriched (12%) neutron-irradiated 6*H*-SiC single crystals were used.

The EPR and ENDOR spectra were detected at *X*- (9.4 GHz) and *W*- (94 GHz) bands on a continuous wave and pulse (electron spin echo, ESE) spectrometers in the temperature range of 1.2–300 K. The samples, in the shape of platelets, had dimension of about $3 \times 4 \times 0.4\text{mm}^3$ for *X*-band and sizes of $0.3 \times 0.4 \times 0.4\,\text{mm}^3$ for *W*-band EPR experiments. The orientation study was facilitated by the possibility to mount the crystal with a high precision owing to the fact that the crystal was cut perpendicular to the *c* axis and to the fact that the cleaved edge of the sample allowed for a precise rotation in the {11-20} plane. Diode lasers operating at 780 or 808 nm were used to excite the samples directly in the spectrometer cavity through phonon-assisted absorption. All numerical simulations of measured data were made using VISUAL EPR software which performs numerical diagonalization of the spin Hamiltonian matrix [55].

III. RESULTS

The family of vacancy-related spin-3/2 centers has the axial symmetry along the *c* axis of hexagonal or orthorhombic SiC polytype. The hyperfine structure parameters arising from such interactions according to the EPR results [56] are presented in Table II. For spin-3/2 centers, optical excitation leads to alignment of the electron spin in the ground state through an effective spin-dependent intersystem crossing pathway.

The fine-structure parameter *D* differs from zero, and has both a positive and a negative sign for different centers. EPR experiments at low temperatures and at a high operating frequency give information about the sign of *D* parameter [22,57]. See Supplemental Material [58] (Fig. S1) for EPR spectra of V2 and V1/V3 centers observed at *X* band in 6*H*-SiC. For several spin-3/2 centers in 15*R*-SiC, as shown below, the signs of the corresponding fine-structure splitting were determined from the ENDOR data.

A. Spin-3/2 color centers in 6*H*-SiC single crystal

Figure 1 shows ESE-detected ENDOR spectra at *W* band of the V2 and V1/V3 centers in 6*H*-SiC, recorded in orientation $B||c$ measured in a wide frequency range. The ENDOR magnetic fields correspond to the high-field (hf) transitions indicated in optically induced ESE-detected EPR spectra shown at the right.

The EPR spectra of the spin centers in SiC can be described by a spin Hamiltonian of the form [59,60]

$$\hat{H} = g_e \mu_B \vec{B} \cdot \vec{S} + D\left[\hat{S}_z^2 - \frac{1}{3}S(S+1)\right] + \sum_i (\vec{S} \cdot \overleftrightarrow{A}_i \cdot \vec{I}_i - g_{Ni}\mu_N \vec{B} \cdot \vec{I}_i). \quad (1)$$

Here, $\vec{S}$ is the electron spin operator with $S = 3/2$ for color centers, g_e is the isotropic electronic *g* factor of the spin-3/2 center, and μ_B is the Bohr magneton. The first term describes the electron Zeeman interaction and the second term reflects the fine structure for spin-3/2 center with the axial symmetry. The HF structure in EPR and ENDOR spectra of the color centers in SiC can be described by the last terms in the spin Hamiltonian. Here, $\vec{I}_i$ represents the nuclear spin operators for ^{29}Si ($I_{\text{Si}} = 1/2$) or ^{13}C ($I_C = 1/2$) nuclei located at different neighbor shells of the Si sites and C sites, g_{Ni} is a *g* factor of nucleus i (g_{N} is negative for ^{29}Si and positive for ^{13}C), and μ_N is the nuclear magneton. The first term reflects the hyperfine interaction where $\overleftrightarrow{A}_i$ is the tensor of this interaction, which describes the HF interaction with the *i*th Si or C atoms, located at different neighbor shells of the spin color center. HF interactions in the first and the second shells of the Si vacancy are partly resolved in the EPR spectra. The second term describes the nuclear Zeeman interaction for ^{29}Si and ^{13}C nuclei. All calculations of the spin Hamiltonian (1) were made using the VISUAL EPR computer package, written by Grachev [55], which performs numerical diagonalization of the spin Hamiltonian matrix.

ENDOR transition frequencies determined by the selection rules $\Delta M_{\text{S}} = 0$ and $\Delta m_{\text{I}} = \pm 1$ are given by [59,60]

$$\nu_{\text{ENDORi}} = h^{-1}|\text{M}_{\text{S}}[a_{\text{i}} + b_{\text{i}}(3\cos^2\theta - 1)] - g_{\text{Ni}}\mu_{\text{N}}B|, \quad (2)$$

where a_{i} and b_{i} are isotropic and anisotropic parts of the HF interaction with the *i*th nucleus, θ is the angle between the external magnetic field *B* and the HF interaction tensor, $g_{\text{Ni}}\mu_{\text{N}}B/h$ is the Larmor frequency f_{L}. The HF interaction tensor components can be expressed in terms of the isotropic *a* and anisotropic *b* components as $A_{||} = a + 2b$ and $A_{\perp} = a - b$ with axial symmetry around the *p* function axis. Here, $a = (8\pi/3)g_{\text{e}}\mu_{\text{B}}g_{\text{N}}\mu_{\text{N}}|\Psi_{2\text{s}}(0)|^2$ and $b = (2/5)\ g_{\text{e}}\mu_{\text{B}}g_{\text{N}}\mu_{\text{N}}\langle r_{2\text{p}}^{-3}\rangle$, where g_{e} is the electronic *g* factor, and Ψ is unpaired-electron wave function.

In Fig. 1, ENDOR lines with the strongest HF interactions (in absolute value) are marked. There is a mirror reflection of the HF interaction lines with different coordination spheres of silicon relative to the Larmor frequency of ^{29}Si for V2 and V1/V3 centers, which unambiguously indicates opposite signs of fine-structure splitting. The inset shows one EPR line of the V2 center in 6*H*-SiC crystal with a natural isotope silicon content and with a modified isotopic composition of silicon (0.7% of ^{29}Si isotope). The satellite lines observed in the EPR spectra are due to the HF interactions with 12 Si atoms located in the next-nearest neighbor (NNN) of a silicon vacancy V_{Si}^-. These lines correspond to the maximum hyperfine interactions with silicon nuclei and labeled as Si_{NNN} in ENDOR spectra. Almost isotropic hyperfine interaction with the ^{29}Si are visible both in EPR and in ENDOR. In EPR spectra the interaction with different Si_{NNN} atoms of the second shell is not distinguishable, whereas in the ENDOR spectra these lines are resolved and are isotropic within the widths of the ENDOR lines. It follows from formula (2) that the HF interaction constant is positive and corresponds a negative spin density (as the nuclear *g* factor g_{N} is negative for ^{29}Si). This observation agrees with the results of the theoretical calculation for isolated silicon vacancy in regular defect-free environment V_{Si}^- [49]. Signals for silicon atoms are visible with HF structure constants designated as A_{i}.

Figure 2 shows *W*-band angular dependence ESE-detected EPR [Fig. 2(a)] and corresponding ESE-detected ENDOR [Fig. 2(b)] spectra of the optically aligned V2 color centers in single 6*H*-SiC crystal. The expanded-scale ESE-detected ENDOR spectrum from Fig. 2(b) is presented in Fig. 2(c). The EPR transitions for the low-field (lf) and high-field magnetic

TABLE II. Ligand hyperfine parameters for interaction with ^{13}C atoms surrounding a spin color center of V1, V2, V3, and V4 in three polytypes of SiC: 6*H*-, 15*R*-, and 4*H*-SiC. The HF interaction with four C atoms located in the NN of a silicon vacancy has axial symmetry along the bonding direction; therefore, parameters are given parallel to the bond ($A_{||}$) and perpendicular to the bond ($A_{\perp}$), from EPR data [56]. The isotropic spin density (s) and anisotropic spin density (p) on C atoms surrounding spin-3/2 centers in three polytypes of SiC: 6*H*-, 15*R*-, and 4*H*-SiC.

Crystal	Center	Atom position	HF interaction for ^{29}Si, ^{13}C (MHz)	a and b (MHz)	Spin density (%)
6*H*-SiC	V2	$C_{NN}(1-4)$	Along the c axis (1) $A_{\|\|} = 80.1$,	$a = 51.7$	$s = 1.34$
		$[C_I]$	$A_{\perp} = 37.5$	$b = 14.2$	$p = 13.4$
		From EPR [56]	Off the c axis (2-4) $A_{\|\|} = 80.1, A_{\perp} = 30.8$	$a = 47.2$	$s = 1.22$
				$b = 16.4$	$p = 15.5$
					$\Sigma = +64.9$
		C_{II}	$B\|\|c$: 2.5		
			$B\|\|c$: 1.9, 1.5		
		C_{III}	$A_{\|\|} \cong 0.562, 0.542,$	$a = 0.39$–0.38	$s \cong 0.01$
			$A_{\perp} \cong 0.31$	$b = 0.087$	$p = 0.82$
		C_{IV}	$-0.48, -0.18$ almost isotropic	$a = -0.48, -0.18$	$s = -0.012, -0.005$
		C_V	0.278, 0.257	$a = 0.28, 0.26$	$s \cong 0.007$
	V1/V3	$C_{NN}(1-4)$	V1		
		$[C_I]$	Along the c axis (1) $A_{\|\|} = 71.7, A_{\perp} = 31.9$	$a = 45.2$	$s = 1.17$
		From EPR [56]	Off the c axis along the bonding	$b = 13.3$	$p = 12.6$
			direction (2-4) $A_{\|\|} = 80.1, A_{\perp} = 30.2$		$s = 1.21$
				$a = 46.8$	$p = 15.7$
				$b = 16.6$	$\Sigma = +64.5$
			V3		$s = 1.20$
			Along the c axis (1) $A_{\|\|} = 80.1, A_{\perp} = 29.7$	$a = 46.5$	$p = 15.9$
			off the c axis along the bonding direction "z" (2-4)	$b = 16.8$	$s = 1.20$
			$A_{\|\|z} = 74.8, A_{\perp y\langle 11-20\rangle} = 26.9, A_{\perp x} = 37.5,$	$a = 46.4$	$p = 13.4$
			$A_{\perp} \cong (A_{\perp y} + A_{\perp x})/2 = 32.2$	$b = 14.2$	$\Sigma = +60.9$
		C_{II}	$B\|\|c$: 4.3, 4.2		
			$B\|\|c$: 2.5		
			$B\|\|c$: 1.6, 1.5		
		C_{III}	0.5		
		C_{IV}	$B\|\|c$: -1.0		$s \cong -0.025$
			-0.47,	$a = -0.47$	$s \cong -0.012$
			-0.28 (almost isotropic)	$a = -0.28$	$s \cong -0.007$
15*R*-SiC	V2	$C_{NN}(1-4)$	$A_{\|\|} = 84.6, A_{\perp} = 33.6$	$a = 50.6$	$s = 1.31$
		$[C_I]$		$b = 17.0$	$p = 16.1$
					$\Sigma = +69.6$
	V3	$C_{NN}(1-4)$ $[C_I]$	From EPR as for V2		
	V4	$C_{NN}(1-4)$ $[C_I]$	From EPR as for V2		
4*H*-SiC	V1	$C_{NN}(1-4)$	Along the c axis (1)	$a = 45.2$	$s = 1.17$
		$[C_I]$	$A_{\|\|} = 71.7, A_{\perp} = 31.9$	$b = 13.3$	$p = 12.6$
		From EPR [56]	Off the c axis (2-4) $A_{\|\|} = 78.4,$	$a = 47.1$	$s = 1.22$
			$A_{\perp} = 31.4$	$b = 15.7$	$p = 14.9$
					$\Sigma = +62.1$
	V2	$C_{NN}(1-4)$	Along c axis $A_{\|\|} = 82.9,$	$a = 50.8$	$s = 1.31$
		$[C_I]$	$A_{\perp} = 34.7$	$b = 16.1$	$p = 15.2$
		EPR [56]	Off c axis $A_{\|\|} = 75.6, A_{\perp} = 29.1$	$a = 44.6$	$s = 1.15$
				$b = 15.5$	$p = 14.6$
					$\Sigma = +63.8$
		C_{II}	4.5–1.5		
		C_{III}	0.6, 0.5	$a \cong 0.6, 0.5$	$s \cong 0.015$
		C_{IV}	Low-intensity signals		$s < 0$

fields are indicated in optically induced ESE spectra. The dotted lines in Figs. 2(b) and 2(c) correspond to the signals recorded in the additional 6*H*-SiC sample under the changed experimental conditions. Intense ENDOR lines are visible in $B||c$, weakly manifested in the main sample because of a blind spot effect [61–63]; see Supplemental Material (Fig. S2) [58]. The angular dependencies of the ENDOR lines are highlighted in gray. Two types of HF interactions were directly observed in the ESE-detected EPR spectra. The first type of the HF interactions occurs with the ^{13}C nuclei located

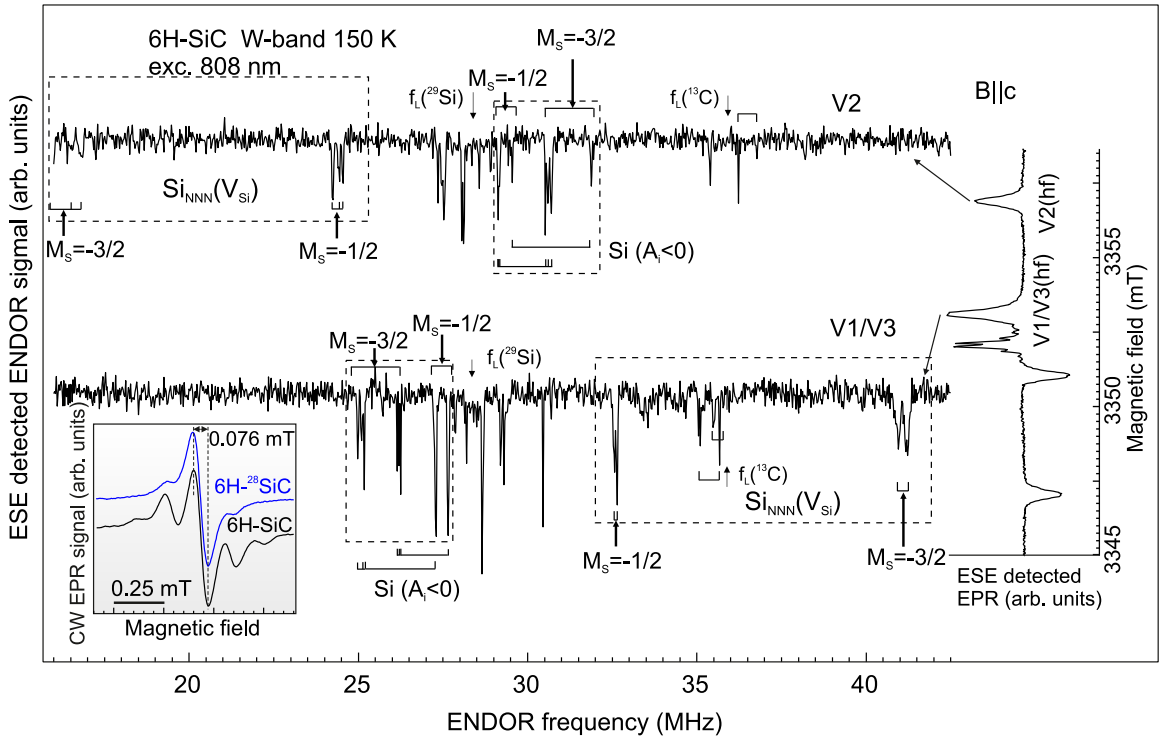

FIG. 1. ESE-detected ENDOR spectra at *W* band of the V2 and V1/V3 centers in 6*H*-SiC, $B||c$, recorded with a scan in a wide frequency range, for the hf transitions indicated in optically induced ESE-detected EPR spectra shown at the right. The ENDOR lines with the strongest HF interactions (in absolute value) are marked. There is a mirror reflection of the HF interaction lines with different coordination spheres of silicon relative to the Larmor frequency of ^{29}Si, which unambiguously indicates opposite signs of fine-structure splitting. The inset shows one EPR line of V2 center in 6*H*-SiC crystal with a natural isotope silicon content and with a modified isotopic composition of silicon (0.7% of ^{29}Si isotope).

in the nearest-neighbor (NN) shell to the V_{Si}^- site. They are strongly anisotropic and reflect the tetrahedral symmetry of the nuclear spin locations. The inset in Fig. 2(a) displays the corresponding anisotropic hyperfine structure. Almost isotropic hyperfine structure induced by the NNN Si atoms with respect to the negatively charged silicon vacancy V_{Si}^- is also shown. $^{13}C_1$ denotes the interaction with the carbon atom oriented along the c axis and $^{13}C_{2-4}$ denotes the interactions with atoms located in the basal plane with the bonds inclined by the angle $\theta = 71^\circ$ relative to the c axis. The HF structure parameters arising from such interactions with ^{13}C nuclei are presented in Table II according to Ref. [56].

There are two types of main HF interactions with silicon ^{29}Si nuclei, which differ in magnitude, sign, and anisotropy. In Fig. 2(b), the signals at $f_L - 1/2|A_{SiNNN}|$ and $f_L - 3/2|A_{SiNNN}|$ correspond to HF interactions with the NNN Si atoms with respect to the negatively charged silicon vacancy V_{Si}^-. All the lines are grouped together because of the almost isotropic hyperfine interaction. The light-induced inverse population of the spin sublevels of V2 centers is shown in the inset. The HF structure parameters arising from such interactions with ^{29}Si nuclei are presented in Table III.

Figure 3 shows an angular dependence of *W*-band ESE-detected ENDOR for the V2 color centers in single 6*H*-SiC crystal. Hyperfine interactions with the surrounding silicon nuclei ^{29}Si (the left-hand side) and carbon ^{13}C (the right-hand side) are presented. The angular dependencies of the ENDOR lines are highlighted in gray and by dashed lines. If the spin density $\rho_S = \Sigma(|\Psi_{s\uparrow}|^2 - |\Psi_{s\downarrow}|^2)$ is the same in sign (for example, $\rho_S < 0$ as in 12 Si_{NNN} atoms), then the HF structure constant $A_S \infty g_N(^{29}Si) > 0$ and $A_S(^{13}C) < 0$ since $g_N(^{29}Si) = -1.1106 < 0$ and $g_N(^{13}C) = 1.404\,82 > 0$. As a result of expression $\nu_{ENDOR} = h^{-1}|M_S A - g_N \mu_N B|$, for the same sign of the spin density, the ENDOR lines of ^{29}Si and ^{13}C are shifted to the same side with respect to the Larmor frequency. For the upper spectrum in Fig. 3, anisotropic signal for ^{13}C (about 0.5 MHz) to the right of Larmor frequency ^{13}C corresponds to a positive spin density, as well as an anisotropic signal for ^{29}Si (about 2.5 MHz) to the right of Larmor frequency ^{29}Si. The signals to the left of the Larmor frequency of ^{29}Si and the Larmor frequency of ^{13}C correspond to negative spin density and partly refer to Si_{NNN} (V_{Si}^-). See Supplemental Material [58] for *W*-band angular dependence ESE-detected EPR spectra of the V2 color centers in single 15*R*-SiC crystal [64].

Figure 4 shows *W*-band angular dependence ESE-detected EPR [Fig. 4(a)] and ESE-detected ENDOR [Fig. 4(b)] spectra of the optically aligned V1/V3 color centers in single 6*H*-SiC crystal. In the $B||c$ orientation, the ESE-detected ENDOR spectrum is additionally presented, recorded from the low-field EPR line under conditions of optical pumping in a *6*H-SiC crystal enriched with the ^{13}C isotope (12%). As a result, the concentration of ^{13}C nuclei is increased by about an order of magnitude and the transitions associated with hyper-

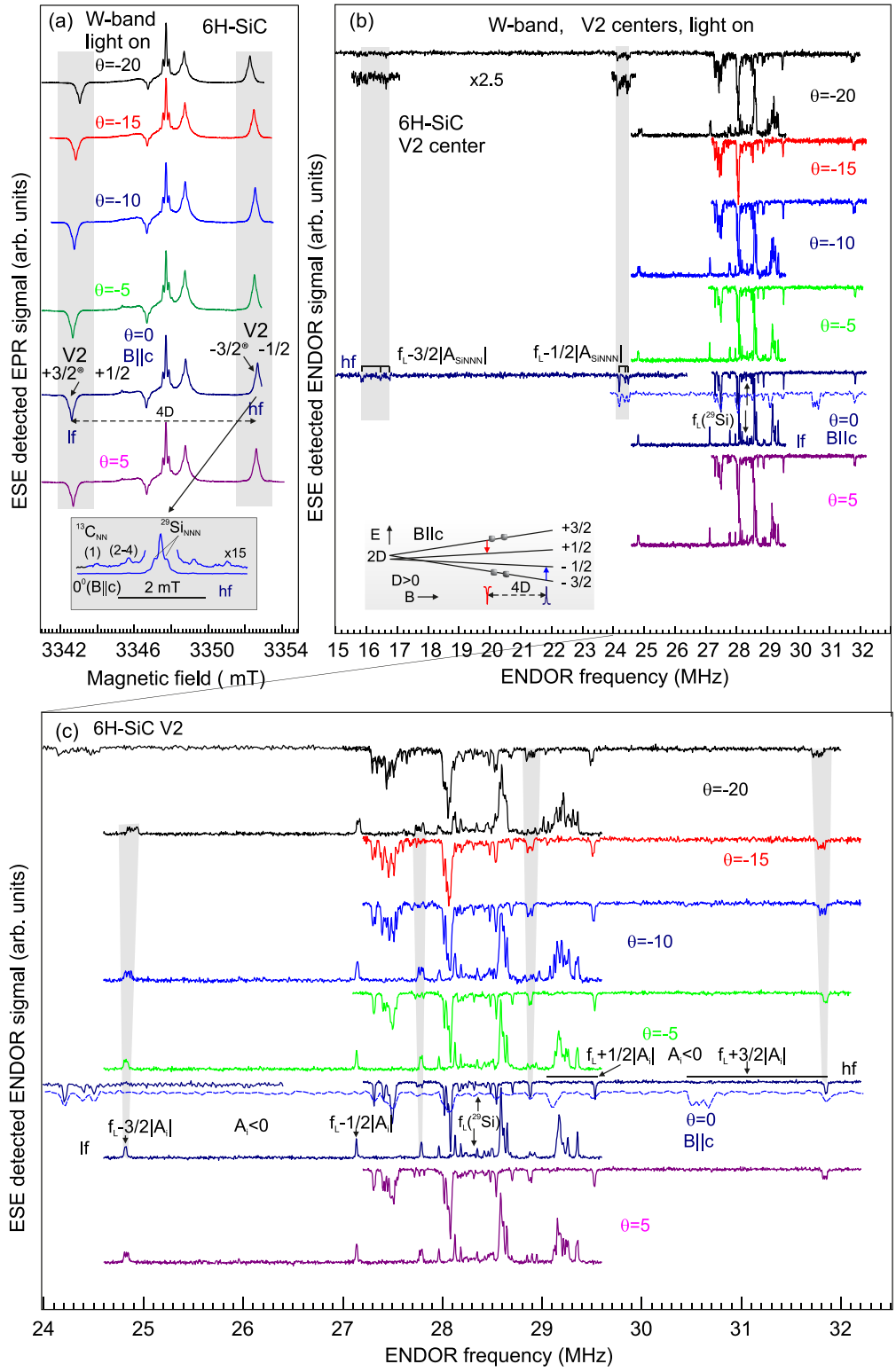

FIG. 2. *W*-band angular dependence ESE-detected EPR (a) and corresponding ESE-detected ENDOR (b) spectra of the optically aligned V2 color centers in single 6*H*-SiC crystal. (c) Expanded-scale ESE-detected ENDOR spectrum from (b). The EPR transitions for the lf and hf magnetic fields are indicated in optically induced ESE spectra. The dotted lines in (b), (c) correspond to the signals recorded in the additional 6*H*-SiC sample. The angular dependencies of the ENDOR lines are highlighted in gray. (b) The signals at $f_L \pm 1/2|A_{SiNNN}|$ and $f_L \pm 3/2|A_{SiNNN}|$ correspond to HF interactions with the NNN Si atoms (with ^{29}Si nuclei) with respect to the negatively charged silicon vacancy V_{Si}^-. The light-induced inverse population of the spin sublevels of V2 centers is shown in the top inset. Bottom inset displays EPR spectrum demonstrating resolved anisotropic hyperfine structure originates from NN carbon atoms (with ^{13}C nuclei) with respect to negatively charged silicon vacancy V_{Si}^-; and almost isotropic hyperfine structure for the next-nearest neighbors Si atoms (with ^{29}Si nuclei) with respect to the negatively charged silicon vacancy VSi V_{Si}^-.

TABLE III. Ligand hyperfine parameters for interaction with ^{29}Si atoms surrounding a spin color center of V1, V2, V3, and V4 in three polytypes of SiC: 6*H*-, 15*R*-, and 4*H*-SiC. The HF interaction with the 12 Si atoms located in the next-nearest neighbor of a silicon vacancy (NNN shell) is almost isotropic (EPR data [56]). The isotropic spin density (s) and anisotropic spin density (p) on Si atoms surrounding spin-3/2 centers in three polytypes of SiC: 6*H*-, 15*R*-, and 4*H*-SiC.

Crystal	Center	Atom	HF interaction for ^{29}Si, ^{13}C (MHz)	a and b (MHz)	Spin density (%)
6*H*-SiC	V2	Si_{NNN} (1-12)	$A = 7.84$	$a = 7.84$	−0.18
		[Si_I]	EPR [56]		−0.17
			$A \approx a = 8.31, 7.92, 7.71$	$a = 8.31, 7.92,$	−0.16
			ENDOR	$7.71 \cong 8.0$	$\Sigma = -2.0$
		Si_{II}	$A_{\|\|} = -2.33; -2.32, -2.31,$	$a = -1.72, -1.71, -1.68;$	$s = 0.037 - 0.036$
			$A_\perp \cong -1.42; -1.40; -1.36$	$b = -0.32, -0.31, -0.3$	$p = 0.28 - 0.26$
		Si_{III}	$A_{\|\|} = 0.71, A_\perp \cong 0.40$	$a = 0.5\ b = 0.1$	$s = -0.011$
			$A_{\|\|} = 0.65, A_\perp \cong 0.39$	$a = 0.48\ b = 0.09$	−−0.010
			$A_{\|\|} = 0.61, A_\perp \cong 0.38$	$a = 0.46\ b = 0.08$	$p = -0.01$
			$A_{\|\|} = 0.58, A_\perp \cong 0.38$	$a = 0.45\ b = 0.07$	−−0.007
			$A_{\|\|} = 0.57, A_\perp \cong 0.38$		
		Si_{IV}	$A \approx a$: −0.34, −0.22	$a \approx -0.34, -0.22$	$s = 0.007$–0.005
		Remote Si shells	0.26, 0.18, 0.12	$a \approx 0.26, 0.18, 0.12$	$s = -0.006$– − 0.003
	V1/V3	Si_{NNN} (1-12)	V1		
		[Si_I]	$A = 8.15$ EPR [56]	$a = 8.15$	$s = -0.21$
			V3		$\Sigma = -2.52$
			$A = 8.4$ EPR [56]	$a = 8.4$	$s = -0.18$
					$\Sigma = -2.16$
			$A = 8.58, 8.38$ ENDOR	$a = 8.58, 8.38$	$s = -0.22$
					$s = -0.21$
					$\Sigma \cong -2.6$
		Si_{II}	$A_{\|\|} = -2.22; -2.15$	$a = -1.64, -1.62;$	$s \cong 0.035$
			$A_\perp \cong -1.35$	$b = -0.29, -0.27$	$p \cong 0.25$
		Si_{III}	$B\|\|c$, 0°		s≈−0.02–−0.015,
			0.664, 0.635, 0.567, 0.38		
			20°		s≈−0.013–−0.008
			0.735, 0.702, 0.659, 0.629,		
			0.582, 0.548, 0.522, 0.493,		
			0.417, 0.371, 0.341, 0.313		
			(small anisotropy)		
		Si_{IV}	−0.47, −0.33	$a = -0.47,$	$s \cong 0.01$
			Anisotropy less 0.5%	−0.33	$s \cong 0.007$
		Remote Si shells	−0.05		$s < 0.001$
15*R*-SiC	V2	Si_{NNN}	$A = 8.35, 8.03, 7.92, 7.75, 7.69$	$a \approx 8.35, 8.03, 7.92, 7.75, 7.69$	$s = -0.18,$
		(Si_I)	Almost isotropic		−0.17,
					−0.16
					$\Sigma = -2.04$
		Si_{II}	$A_{\|\|} \cong -2.34;$	$a = -1.72, -1.71;$	$s = 0.036,$
			$A_\perp \cong -1.43, 1.40$	$b = -0.3, -0.31$	$p = 0.26$–0.27
		Si_{III}	$A_{\|\|} = 0.71, A_\perp \cong 0.42$	$a = 0.52\ b = 0.097$	$s = -0.011$–−0.010,
			$A_{\|\|} = 0.64, A_\perp \cong 0.42$	$a = 0.49\ b = 0.07$	
			$A_{\|\|} = 0.58, A_\perp \cong 0.41$	$a = 0.47\ b = 0.06$	$p = -0.087$–−0.061
			$A_{\|\|} = 0.57, A_\perp \cong 0.41$	$a = 0.47\ b = 0.06$	
		Si_{IV}	$A = -0.34, -0.23$ (almost isotropic)	$a \approx -0.34, -0.23$	$s = 0.007, 0.005$
		Remote Si shells	0.26, 0.18, 0.12 (almost isotropic)	$a \approx 0.26, 0.18, 0.12$	$s = -0.005$–−0.002
	V3	Si_{NNN}	From EPR approximately as		
		(Si_I)	for V2		
		Si_{II}	∼10°		
			−2.33, −2.21, −2.13, −1.49,	$a \approx -1.67, -1.6;$	$s \cong 0.035$
			−1.46, −1.41	$b \approx -0.27, -0.25$	$p \cong 0.23$
			($A_{\|\|} \cong -2.22$−2.22, −2.20, −2.10;		
			$A_\perp \cong -1.40$−1.40, −1.35)		
		Si_{III}	∼10° 0.68, 0.66, 0.64, 0.62, 0.59,		
			0.55, 0.54, 0.51, 0.4		

TABLE III. *(Continued.)*

Crystal	Center	Atom	HF interaction for ^{29}Si, ^{13}C (MHz)	a and b (MHz)	Spin density (%)
		Si_{IV}	$A \approx -0.44, -0.33, -0.32$	$a \approx -0.44, -0.33, -0.32$	$s = 0.009, 0.007$
		Remote Si shells	0.2		$s = -0.003$
	V4	Si_{NNN}	From EPR approximately as for V2		
		Si_{II}	~10°: −2.3, −2,13, −2.11		Spin density >0
		Si_{III}	~10°: 1.3, 0.70, 0.67, 0.65, 0.62, 0.55, 0.53		Spin density <0
		Si_{IV}	~10°: −0.50, −0.47, −0.34, −0.32		Spin density >0
		Remote Si shells	0.28, 0.12		Spin density <0
4*H*-SiC	V1	Si_{NNN} (V_{Si}^-)	$A = 8.15$	$a = 8.15$	$s = -0.21$
		From EPR [56]			$\Sigma = -2.52$
	V2	Si_{NNN}	$A = 8.34$ EPR [56]	$a = 8.34$	$s = -0.215$
		(Si_I)	$A = 8.81, 8.74, 8.62, 7.90$ ENDOR	$a \approx 8.8, 8.7, 8.6, 7.9$	$\Sigma = -2.58$
					$s = -0.23, -0.225, -0.22, -0.20$
					$\Sigma \approx -2.6$
		Si_{II}	$A_{\|\|} = -2.3, -2.14$ $A_\perp = -1.5$	$a = -1.77, -1.71$ $b = -0.27, -0.21$	$s = 0.037$–0.036; $p \approx 0.23$
		Si_{III}	$A = 1.307, 1.292, 0.743, 0.719, 0.702, 0.671, 0.620, 0.605, 0.569, 0.524, 0.521$ (small anisotropy)	$a = 1.307, 1.292, 0.743, 0.719, 0.702, 0.671, 0.620, 0.605, 0.569, 0.524, 0.521$	$s = -0.034, -0.034, -0.019$–$-0.018, -0.017$–$-0.016, -0.015$–$-0.013$
		Si_{IV}	$A = -0.5, -0.468, -0.447, -0.367, -0.32$	$a \approx -0.5, -0.468, -0.447, -0.367, -0.32$	$s = 0.01$–0.007
		Remote Si shells	0.11	$a \approx 0.1$	$s = -0.003$

fine interactions with ^{13}C are sharply enhanced, which made it possible to reliably register ENDOR and determine the constants of this interaction (see Table II). The expanded-scale ESE-detected ENDOR spectrum from Fig. 4(b) is presented in Fig. 4(c). The EPR transitions for the low-field and high-field magnetic fields are indicated in optically induced ESE spectra.

As in the previous figures, in Fig. 4(b) the signals at $f_L + 1/2|A_{SiNNN}|$ and $f_L + 3/2|A_{SiNNN}|$ correspond to HF interactions with the next-nearest neighbors Si atoms with respect to the negatively charged silicon vacancy V_{Si}^-. The light-induced inverse population of the spin sublevels of V1/V3 centers ($D < 0$) is shown in the top inset. Bottom inset displays expanded-scale ESE-detected ENDOR signals due to an almost isotropic hyperfine interaction with carbon atoms (with ^{13}C nuclei).

B. Spin-3/2 color centers in 15*R*-SiC single crystal

Figure 5 shows ESE-detected ENDOR spectra at *W* band of the V2 centers in 15*R*-SiC, $B \sim ||c$ for the low-field and high-field transitions in optically induced ESE-detected EPR spectra. In Fig. 6, the ESE-detected ENDOR spectra at *W* band on an enlarged scale of the V2, V3, and V4 spin-3/2 centers in 15*R*-SiC are presented (the ENDOR spectra for V2 centers are given for comparison). The spectra are measured at orientation $\theta \approx 10^\circ$ for the lf and hf transitions indicated in optically induced ESE spectra shown at the right. The insets show the schemes of energy levels and their optically induced populations for the studied spin-3/2 centers. It is seen that the levels with $M_S = \pm 3/2$ are predominantly populated; that is, taking into account the positive sign of the fine structure ($D > 0$), an optically induced inverse population of the spin sublevels is observed at room temperature even in a zero magnetic field.

Let us consider in more detail the ENDOR spectra of the V3 and V4 centers. On the basis of the ENDOR research, taking into account that only the sign of the fine structure for V2 centers is known from the EPR studies, the scheme of the energy levels and population of these levels under the action of optical pumping can be constructed. As a basis, we take the similarity of the ENDOR spectra for hyperfine interactions with silicon nuclei ^{29}Si surrounding the silicon vacancy. These interactions are characterized by a positive sign of the hyperfine structure constant (i.e., a negative spin density on silicon nuclei), as was shown on the basis of studies of V2 centers. Thus, M_S for EPR transitions in high and low fields are identified, which are included in Eq. (2) for determining the frequencies of the ENDOR lines.

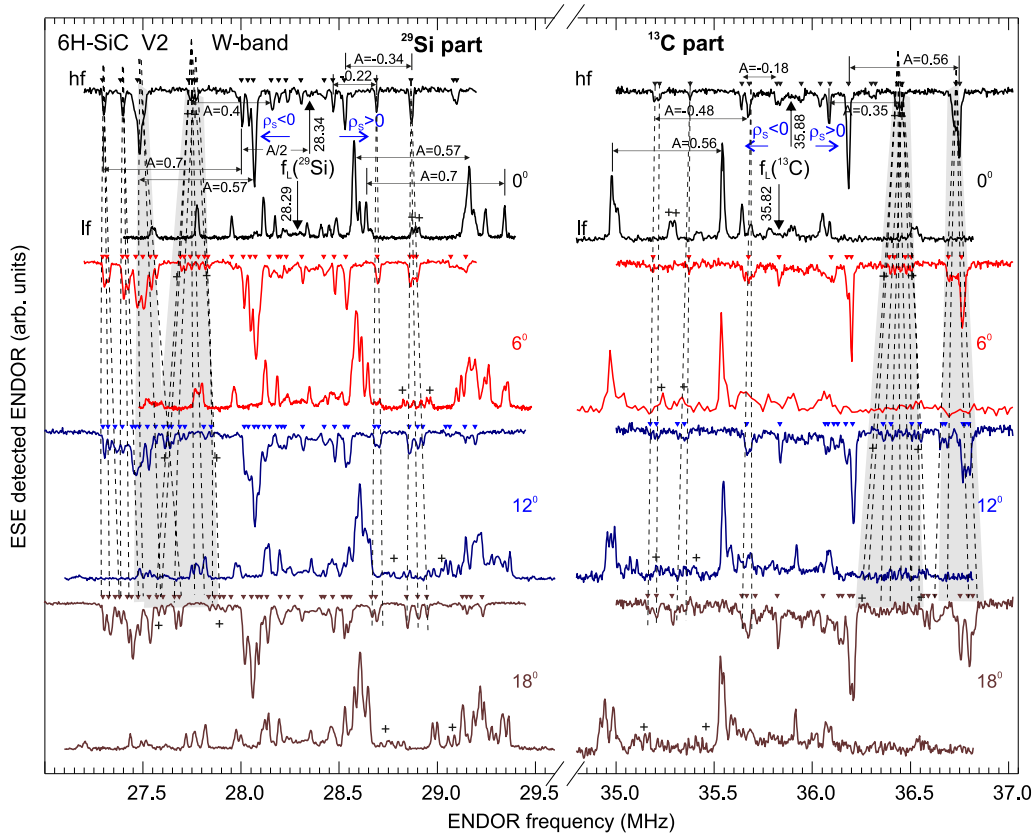

FIG. 3. Angular dependence of *W*-band ESE-detected ENDOR for V2 color centers in single 6*H*-SiC crystal. Hyperfine interactions with the surrounding silicon nuclei ^{29}Si (left-hand side) and carbon ^{13}C (right-hand side) are presented. The angular dependencies of the ENDOR lines are highlighted in gray and by dashed lines.

First, we compare the relative position of the EPR lines in the magnetic field and the position of the ENDOR lines with respect to the Larmor frequency for the V2 center on one side (which is known) and the V3 and V4 centers under consideration (the V1 center is not considered, since we did not find the EPR spectrum corresponding to the zero-phonon line V1). This information in the future, after establishing the order of energy levels (sign D), will make it possible to find populations of spin sublevels under the action of optical pumping. Figure 6 shows that the low-field lines V2 and V4 correspond to ENDOR signals for interaction with silicon nuclei with a positive HF constant located in the frequency range above the Larmor frequency, whereas for V2 and V3, the ENDOR signals correspond to the interaction with silicon nuclei with a positive HF interaction constant, located in the range above and below the Larmor frequency. This gives us reason to state that for V2 and V4 low-field and high-field transitions correspond to the same values of M_S; that is, in both cases the sign of D is the same ($D > 0$). For V3 centers, the opposite situation is observed; that is, the D sign is negative ($D < 0$). These results are reflected in the corresponding insets, where the energies of spin sublevels in a magnetic field for the V4 and V3 centers are given. A population of the spin sublevels is obtained on the basis of the EPR-signal position with an inverted phase in the magnetic field, that is, the signal of microwave radiation (Fig. 6).

C. Spin-3/2 color centers in 4*H*-SiC single crystal

Figure 7 presents ESE-detected ENDOR spectra at *W* band of the V2 color centers in 4*H*-SiC measured at orientation $\theta \approx 0^\circ$ for the low-field and high-field transitions indicated in optically induced ESE spectra shown at the right. The inset shows the ground-state energy levels diagram for the V2 center in 4*H*-SiC. In the central part of the EPR spectrum, a spin-3/2 center with $D = 0$ absorption signal is seen, which is not optically active. The ENDOR of these centers in 4*H*-SiC was presented in Ref. [49], where a theoretical description of hyperfine interactions with $Si_{NNN}(V_{Si})$ was given and it is shown that the spin density on silicon is negative. To determine the sign of the HF interaction, it is necessary to unambiguously select one of the electronic transitions. For optically active spin-3/2 centers, this results from the alignment of the populations of the spin levels.

The EPR spectra of the spin-3/2 centers with $D = 0$ were studied in all the main polytypes of silicon carbide, including cubic. Based on the study of HF interactions with the 12 Si atoms in the NNN shell in 4*H*-SiC, it was found that the spin is 3/2 [49]. Figure 8 shows ESE-detected EPR [Fig. 8(a)] and ENDOR [Fig. 8(b)] spectra at *W* band of the spin-3/2 centers with $D = 0$ in 15*R*-SiC. It can be seen that these ENDOR lines are symmetrical with respect to the Larmor frequency; that is, they do not have optical alignment and these spectra differ significantly from those shown in Figs. 1–7 which belong

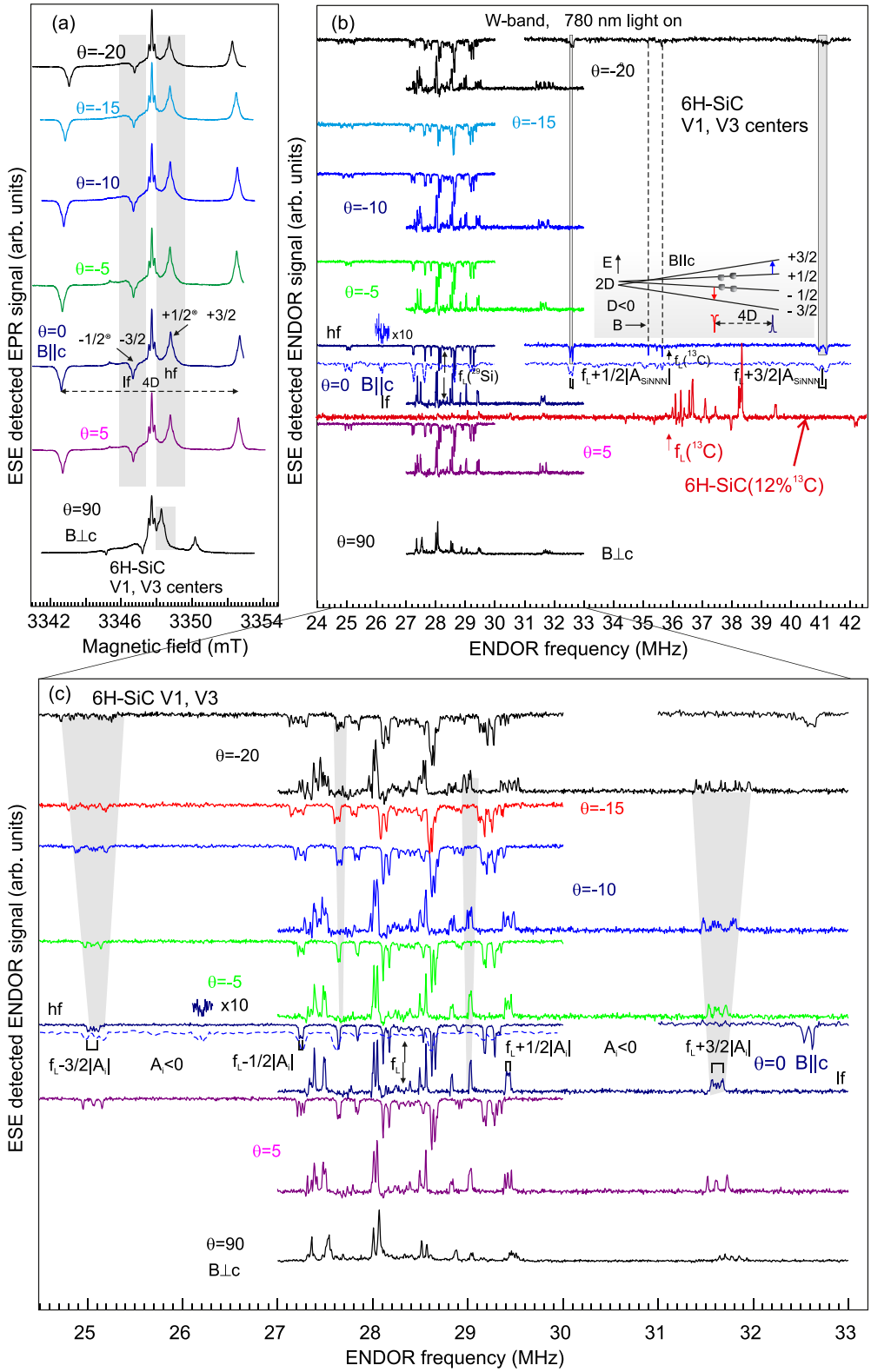

FIG. 4. *W*-band angular dependence ESE-detected EPR (a) and ESE-detected ENDOR (b) spectra of the optically aligned V1/V3 color centers in single 6*H*-SiC crystal. (c) Expanded-scale ESE-detected ENDOR spectrum from (b). The EPR transitions for the low-field and high-field magnetic fields are indicated in optically induced ESE spectra. The signals at $f_L \pm 1/2|A_{SiNNN}|$ and $f_L \pm 3/2|A_{SiNNN}|$ (b) correspond to HF interactions with the next-nearest neighbors Si atoms (with ^{29}Si nuclei) with respect to the negatively charged silicon vacancy V_{Si}^-. (inset) The light-induced inverse population of the spin sublevels of V1/V3 centers ($D < 0$). In the $B||c$ orientation, the ESE-detected ENDOR spectrum is additionally presented, recorded from the low-field EPR line under conditions of optical pumping in a 6*H*-SiC crystal enriched with the ^{13}C isotope (12%). As a result, the transitions associated with HF interactions with ^{13}C are sharply enhanced. The spectra for the perpendicular orientation ($B \perp c$) are given for demonstrating a small orientation dependence for some ENDOR signals.

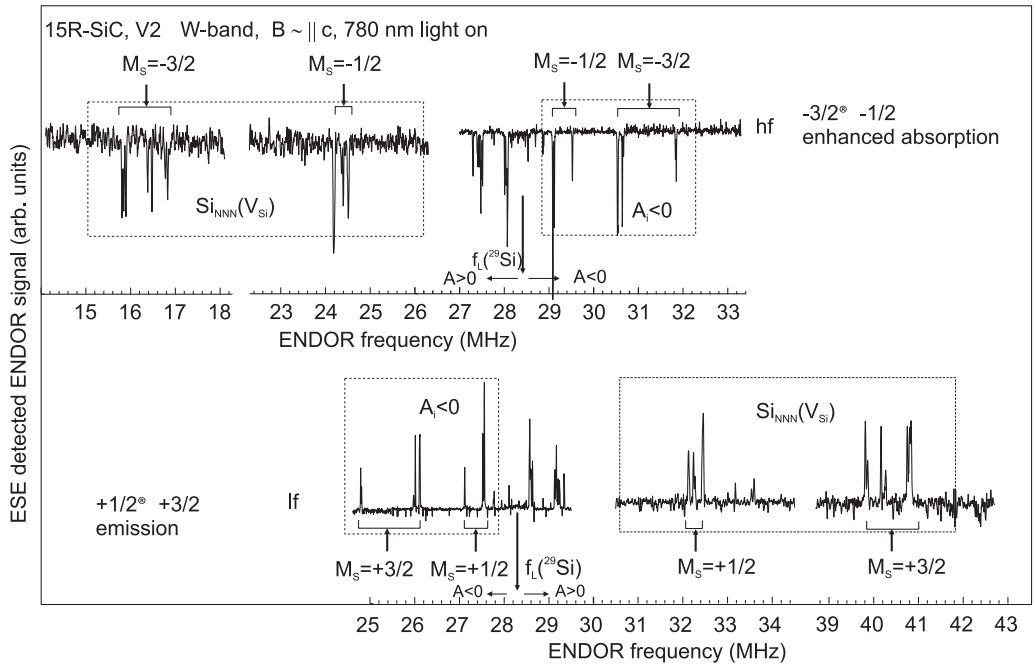

FIG. 5. ESE-detected ENDOR spectra at *W* band of the V2 centers in 15*R*-SiC, $B \sim ||c$ for the low-field and high-field transitions in optically induced ESE-detected EPR spectra. The same designations were used as shown in Fig. 1 for V2 center.

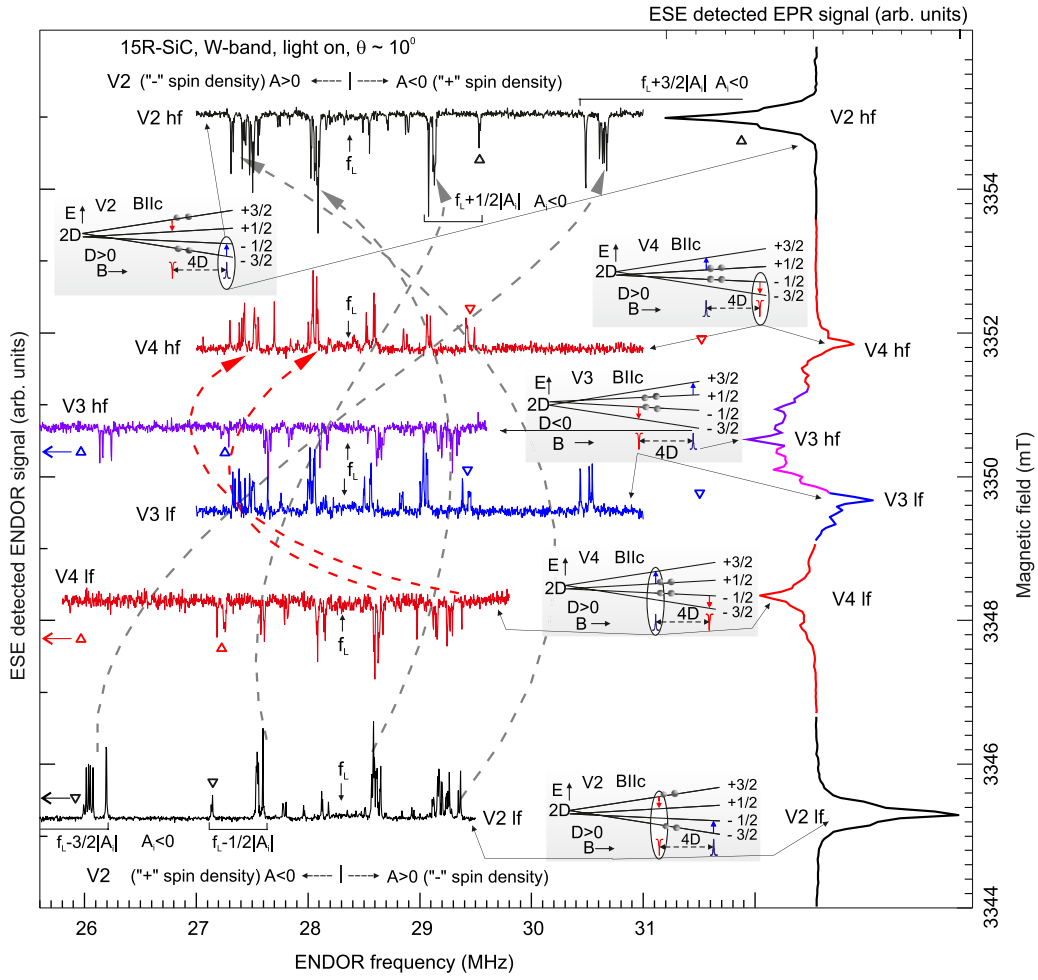

FIG. 6. ESE-detected ENDOR spectra at *W* band of the V2, V3, and V4 color centers in 15*R*-SiC measured at orientation $\theta \approx 10^{\circ}$ for the low-field and high-field transitions indicated in optically induced ESE spectra shown at the right.

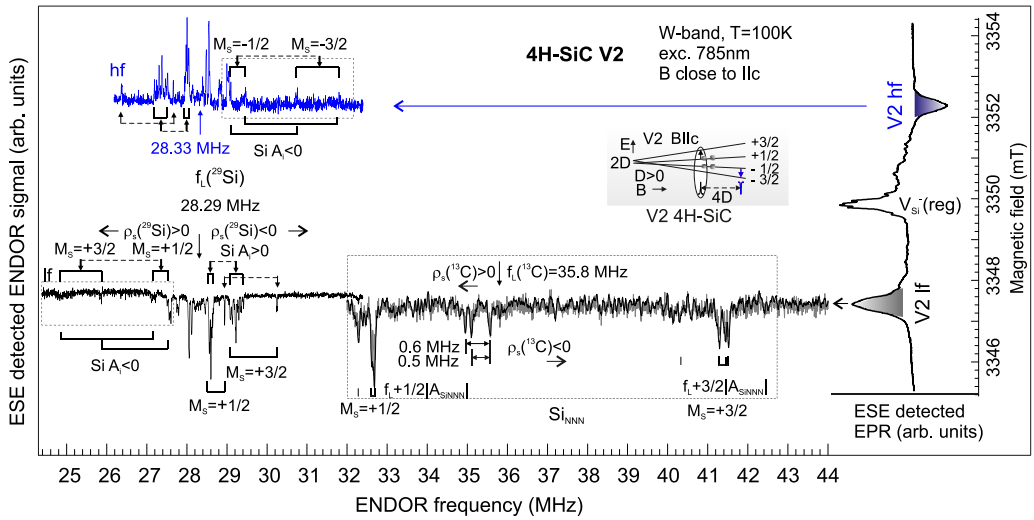

FIG. 7. ESE-detected ENDOR spectra at *W* band of the V2 color centers in 4*H*-SiC measured at orientation $\theta \approx 0^\circ$ for the low-field and high-field transitions indicated in optically induced ESE spectra shown at the right. The inset shows the level system for the V2 center in 4*H*-SiC.

to anisotropic spin $S = 3/2$ color centers with $D \neq 0$. Note that the spin-3/2 centers with $D = 0$ seem to be manifested in spin-dependent recombination in experiments on electrical detection of magnetic resonance [65].

IV. DISCUSSION

We will consider the main features observed in the ESE-detected ENDOR spectra common to all spin-3/2 centers with unique properties of high-temperature optically induced alignment of the spin-level populations (optically active spin-3/2 center) in all silicon carbide polytypes: hexagonal 4*H*-, 6*H*-, and rhombic 15*R*-SiC. The most intense ENDOR lines are observed in the Larmor frequency region of ^{29}Si and ^{13}C nuclei, with signals visible on both sides of the Larmor frequency. The ENDOR signals in optical alignment conditions registered over the low-field and high-field EPR lines have mirror symmetry with respect to the Larmor frequency with phase inverting. A small shift of the ENDOR lines is due to a difference in the Larmor frequency owing to different magnetic fields for the EPR transitions.

The position of all the ENDOR lines in one spectrum is not symmetric with respect to the Larmor frequency. An interaction with each *i*th ^{29}Si and ^{13}C nucleus induces two

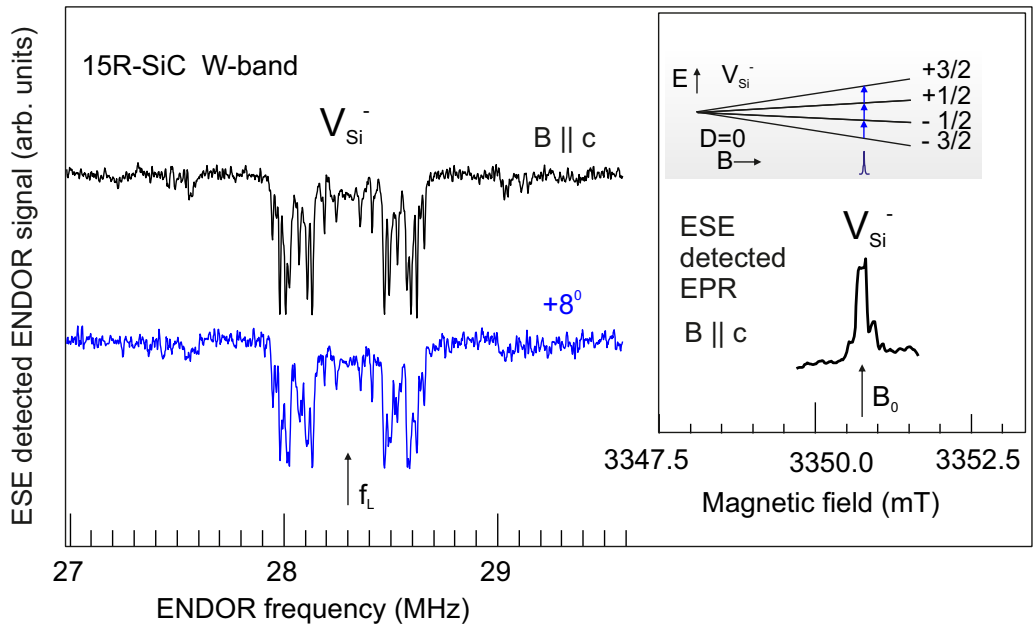

FIG. 8. ESE-detected ENDOR spectra at *W* band of the negatively charged silicon vacancy in regular environment, V_{Si}^- center, in 15*R*-SiC (for two orientations), which are characterized by zero-field splitting $D = 0$. Inset shows the spin-level diagram and ESE-detected EPR for spin-3/2 centers with $D = 0$ (optically not active) in 15*R*-SiC.

sets of ENDOR transitions located at the distances of $1/2A_i$ and $3/2A_i$ from the Larmor frequency f_L. Thus, in all spectra it is possible to distinguish pairs of lines located at a distance of $1/2A_i$ and $3/2A_i$ from the Larmor frequency on either side of the Larmor frequency. A remarkable feature of the spectra for spin-3/2 is the fact that the distance between the two transitions allows one to determine with high accuracy both the HF interaction constant (including HF-constant sign) and the ^{29}Si and ^{13}C Larmor frequency at a fixed magnetic field.

Some of the positions of the ENDOR lines depend on the orientation of the crystal in the magnetic field (angle θ); that is, the lines are anisotropic [see Eq. (2)], and some of the lines are almost isotropic. An important task is to compare the HF interactions and identify those that are observed, both in the EPR spectra and in the ENDOR spectra. Such binding research allows, as a rule, to exclude erroneous interpretation of the ENDOR spectra.

The positive sign of the parameter D for V2 centers in 4*H*-SiC, 6*H*-SiC, and 15*R*-SiC and the negative sign for V1/V3 centers in 6*H*-SiC were established from EPR spectra (see Supplemental Material). The ENDOR measurements confirmed the EPR data and made it possible to determine the signs of the D parameter for other spin centers that were not found in the EPR studies. Using this information it was possible to identify the transitions observed in the EPR spectra and, ultimately, from the position of the signals with the inverted phase in the magnetic field to find optically induced populations of spin sublevels in the ground $S = 3/2$ state. Attention is drawn to the similarity of ENDOR signals for different centers and polytypes: there are always signals with maximum interactions with ^{29}Si nuclei belonging to the second shell around the silicon vacancy—-the next-nearest neighbors NNN (Si_{NNN}). These signals correspond to almost isotropic satellites that appear in the EPR spectra. In contrast to the EPR spectra, there is a set of interactions seen in the ENDOR signals with closely related parameters, since 12 NNN silicon atoms in this shell are slightly nonequivalent.

In accordance with the identified EPR transitions for the V2 centers, due to the known parameter D, for these interactions the HF interaction constant is positive; that is, the sign of the spin density on the silicon nuclei is negative (in view of the negative nuclear g factor for silicon, ^{29}Si). HF interactions with positive HF constants also correspond to a whole set of lines located on the same side relative to the Larmor frequency ^{29}Si as the lines responsible for interactions with 12 silicon atoms Si_{NNN}. These lines are attributed to the interaction with the farther silicon spheres.

The next stage is a consideration of the ENDOR lines located on the opposite side of the ^{29}Si Larmor frequency, therefore having the opposite sign of the HF interaction with ^{29}Si nuclei: in other words, a negative HF interaction value (A_i) corresponding to a positive spin density on the silicon core. A distinctive feature of this interaction is its relatively large magnitude and sharp anisotropy.

Unfortunately, the ENDOR angular dependences were not measured for all orientations, since the ESE-detected ENDOR signal intensity drops with an increase in the angle between the direction of the magnetic field and c-axis orientation. In addition, the EPR lines of different spin-3/2 centers are overlapped for angles approaching 55°. Therefore, for anisotropic spectra, the HF structure tensor quantities were roughly estimated, but, nevertheless, the experimentally found frequencies are accurate and open up wide possibilities for controlling the nuclear spins of ^{29}Si and ^{13}C in qubits based on spin-3/2 centers in SiC. The experimentally discovered opposite signs of hyperfine interactions on ^{29}Si and ^{13}C nuclei are of particular importance for applications (for example, in gyroscopes).

The starting point of our research was to obtain EPR and ENDOR experimental data, unambiguously related to the spin-3/2 centers with unique properties of optically induced alignment of the spin-level populations. The spin-3/2 color centers are defects with deep levels in the band gap; therefore, the wave functions of these centers are quite strongly localized in comparison with shallow donors and shallow acceptors (see Refs. [66–73]). The spin-3/2 centers in polytypes 4*H*-SiC, 6*H*-SiC, and 15*R*-SiC show very similar hyperfine structure. V2 centers have common properties in the three polytypes: zero-field splitting is maximum and the splitting parameter $D > 0$. Tables II and III show ligand hyperfine parameters for interaction with carbon atoms (^{13}C) and silicon atoms (^{29}Si) surrounding a spin-3/2 color center in three polytypes of SiC: 6*H*-, 15*R*-, and 4*H*-SiC. To consider the distribution of s and p character, the observed HF interactions were translated into spin density using the table of Morton and Preston [74]. The isotropic HF interaction (a) gives a measure of the s spin density (s), whereas the anisotropic HF interaction (b) is a measure for the p density (p). The s and p spin densities of the unpaired electron connected to the spin-3/2 centers in SiC with the nuclei surrounding the center are presented in Tables II and III.

In the ENDOR spectra (Figs. 1–7), several groups of lines with similar properties are distinguished, which can be attributed to silicon (^{29}Si) and carbon (^{13}C) atoms occupying close positions (coordination spheres of the same type at approximately the same distances) relative to the central position of a spin-3/2 defect in the form of a negatively charged silicon vacancy V_{Si}^-. These groups are located on both sides of the corresponding Larmor frequencies of ^{13}C and ^{29}Si, unambiguously demonstrating the opposite signs of HF structure constants. As mentioned above, the wave function of the spin-3/2 defect should rapidly decrease in amplitude with increasing distance from the negatively charged silicon vacancy.

One of the tasks is an assignment of lines in the ^{13}C and ^{29}Si ENDOR spectra to specific C and Si atoms up to ten bond lengths away from the silicon vacancy V_{Si}^-. In Tables II and III the groups of C and Si atoms, respectively, are sorted on the basis of the value of the HF interaction. Roman numerals in the form of indices for C and Si indicate the coordination sphere, while only the C or Si spheres are counted. The groups of atoms are divided into subgroups, sometimes containing only one atom. C_I, C_{II}, C_{III}, and C_{IV} correspond to carbon atoms located, respectively, at a distance of one, three, five, and seven molecular bonds from the center of the spin-3/2 defect in the form of a negatively charged silicon vacancy. Si_I, Si_{II}, Si_{III}, and Si_{IV}, correspond to silicon atoms located, respectively, at a distance of two, four, six, and eight molecular bonds from the center of the defect in the form of a silicon

vacancy. Groups of C and Si nuclei indicated by $C_{NN}(1-4)$ and $Si_{NNN}(1-12)$ correspond to the C nearest neighbors (NN) and the Si next-nearest neighbors (NNN) according the silicon vacancy V_{Si}^-. Distance from V_{Si}^- to $C_{NN}(1-4)$ [C_I] in 6*H*-SiC is of 1.88–1.89 Å, that to $Si_{NNN}(1-12)$ [Si_I] is of 3.07–3.09 Å, that to $C_{II}(n)$ is of 4.41, 4.75 Å, etc. (see Refs. [66,67]).

We will take as a basis the positive spin density, starting from the first coordination sphere of carbon. As can be seen from Table II, this sphere accounts for about 65% of the positive spin density. In the second coordination sphere of carbon, spaced from the silicon vacancy by two bonds, indicated as C_{II}, there is a large number of atoms; we assume that they also account for a part of the positive spin density (Table II). The atoms designated as C_{II} are geometrically differently located in the crystal. This arrangement depends on the position of the silicon vacancy in the lattice, therefore, the values of the HF structure constants substantially depend on these positions. A more complicated situation is observed with ^{29}Si, since already in the first shell of silicon (the second coordination sphere, if the first C shell is taken into account), the spin density is negative; that is, the core polarization mechanism is realized [75]. Further, we have groups of lines with positive and negative spin densities, with hyperfine interactions decreasing in absolute value. It turned out that part of the lines was more anisotropic than expected on the basis of a dipole-dipole interaction with the spin density on the silicon vacancy V_{Si}^-. This leads to the conclusion that there is also a direct spin density in the *p* orbitals on the neighboring Si atoms, and that the *z* axis of each HF tensor should be parallel to the bonds.

The extensive ENDOR data for many shells in this paper (Tables II and III) are considered as an experimental demonstration of spin-density oscillations on different coordination spheres of silicon and carbon near the spin-3/2 color center in wide band-gap semiconductors with deep levels in the band gap. The spin-density oscillations were theoretically predicted in the NV^- center in diamond where the hyperfine interactions were obtained by first-principles calculations [76]; the negative spin density for isolated silicon vacancy in the second Si shell was theoretically predicted in 4*H*-SiC [49,77]. In our work, the oscillations of the spin density on ligand atoms in a wide-band semiconductor are demonstrated experimentally. This result can be of fundamental importance for applications.

The experimental HF interaction constants presented in Tables II and III largely correspond to the results from *ab initio* theoretical calculations of the HF interaction constants performed in Refs. [77,78] for a negatively charged silicon vacancy in SiC. Moreover, when identifying various coordination spheres, we took into account the results of these calculations. Thus, the experimental ENDOR data confirm that the core of the spin-3/2 center is a negatively charged silicon vacancy. A more detailed discussion of possible models

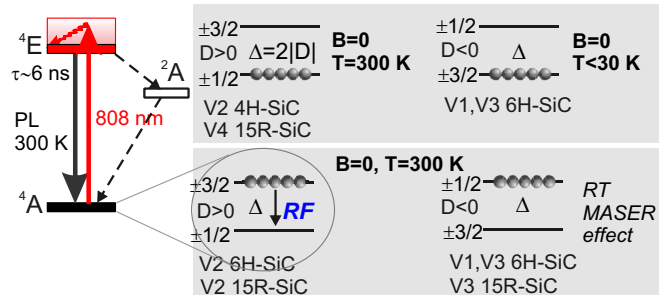

FIG. 9. Optically induced level spin alignment of V1, V2, V3, and V4 centers in 4*H*-, 6*H*-, and 15*R*-SiC.

of spin-3/2 centers appeared in a theoretical paper which was published during the review period of this work (see Ref. [79] and references therein).

On the basis of the EPR and ENDOR investigations, signs of the fine-structure splitting for all the centers were demonstrated, which made it possible to establish the form of optically induced spin alignment, including the inverse populations of the levels for a number of the spin-3/2 centers. Figure 9 demonstrates the optically induced level spin alignment at room temperature and $B = 0$. For V1 and V3 centers in 6*H*-SiC optically induced level spin alignment is also shown at 30 K, $B = 0$.

Summarizing, a number of spin-3/2 color centers differing in the parameters of the fine structure and hyperfine interactions in the ground state have been investigated in 4*H*-SiC, 6*H*-SiC, and 15*R*-SiC single crystals by pulsed high-frequency EPR and ENDOR techniques. The EPR and ENDOR experimental data relate unambiguously to spin-3/2 centers in which the optically induced alignment of the spin-level populations occurs. The hyperfine interaction constants with silicon (^{29}Si) and carbon (^{13}C) nuclei located both in the nearest and distant coordination spheres are determined by the method of high-frequency ESE-detected ENDOR under conditions of optically induced alignment of the spin-3/2 center. The hyperfine interactions with ^{29}Si and ^{13}C nuclei located in different coordination spheres are unambiguously separated due to the selective population of the fine-structure levels with certain values of M_S. The signs of hyperfine interactions with ^{29}Si and ^{13}C nuclei and, as a result, the signs of oscillating spin density, are determined. The form of the optically induced spin alignment, including the level population inversion for a number of spin-3/2 centers, is established.

ACKNOWLEDGMENT

The work was carried out with the financial support of the Russian Science Foundation (Project No. 20-12-00216).

[1] G. Watkins, in *Deep Centers in Semiconductors*, edited by S.T. Pantelides (Gordon and Breach, New York, 1986), p. 147.

[2] A. Gruber, A. Drabenstedt, C. Tietz, L. Fleury, J. Wrachtrup, and C. von Borczyskowski, Scanning confocal optical

microscopy and magnetic resonance on single defect centers, Science **276**, 2012 (1997).
[3] F. Jelezko, T. Gaebel, I. Popa, A. Gruber, and J. Wrachtrup, Observation of Coherent Oscillations in a Single Electron Spin, Phys. Rev. Lett. **92**, 076401 (2004).
[4] R. Hanson, F. Mendoza, R. J. Epstein, and D. D. Awschalom, Polarization and Readout of Coupled Single Spins in Diamond, Phys. Rev. Lett. **97**, 087601 (2006).
[5] F. Jelezko and J. Wrachtrup, Single defect centers in diamond: A review, Phys. Status Solidi A **203**, 3207 (2006).
[6] D. D. Awschalom and M. E. Flatté, Challenges for semiconductor spintronics, Nature Phys. **3**, 153 (2007).
[7] R. Hanson and D. D. Awschalom, Coherent manipulation of single spins in semiconductors, Nature (London) **453**, 1043 (2008).
[8] M. Koenraad and M. E. Flatté, Single dopants in semiconductors, Nat. Mater. **10**, 91 (2011).
[9] P. G. Baranov, I. V. Il'in, E. N. Mokhov, M. V. Muzafarova, S. B. Orlinskii, and J. Schmidt, EPR identification of the triplet ground state and photoinduced population inversion for a Si-C divacancy in silicon carbide, JETP Lett. **82**, 441 (2005).
[10] P. G. Baranov, A. P. Bundakova, I. V. Borovykh, S. B. Orlinskii, R. Zondervan, and J. Schmidt, Spin polarization induced by optical and microwave resonance radiation in a Si vacancy in SiC: A promising subject for the spectroscopy of single defects, JETP Lett. **86**, 202 (2007).
[11] J. R. Weber, W. F. Koehl, J. B. Varley, A. Janotti, B. B. Buckley, C. G. Van de Walle, and D. D. Awschalom, Quantum computing with defects, Proc. Natl. Acad. Sci. USA **107**, 8513 (2010).
[12] D. DiVincenzo, Quantum bits: Better than excellent, Nat. Mater. **9**, 468 (2010).
[13] P. G. Baranov, A. P. Bundakova, A. A. Soltamova, S. B. Orlinskii, I. V. Borovykh, R. Zondervan, R. Verberk, and J. Schmidt, Silicon vacancy in SiC as a promising quantum system for single defect and single-photon spectroscopy, Phys. Rev. B **83**, 125203 (2011).
[14] A. G. Smart, Silicon carbide defects hold promise for device-friendly qubits, Phys. Today **65**(1), 10 (2012).
[15] A. I. Veinger, V. A. Il'in, Yu. M. Tairov, and V. F. Tsvetkov, Investigation of thermal defects in silicon carbide by the ESR method, Sov. Phys. Semicond. **13**, 1385 (1979).
[16] V. S. Vainer and V. A. Il'in, Electron spin resonance of exchange-coupled vacancy pairs in hexagonal silicon carbide, Sov. Phys. Solid State **23**, 2126 (1981).
[17] H. J. von Bardeleben, J. L. Cantin, I. Vickridge, and G. Battistig, Proton-implantation-induced defects in n-type 6H- and 4H−SiC: An electron paramagnetic resonance study, Phys. Rev. B **62**, 10126 (2000).
[18] H. J. von Bardeleben, J. L. Cantin, L. Henry, and M. Barthe, Vacancy defects in p-type 6H−SiC created by low-energy electron irradiation, Phys. Rev. B **62**, 10841 (2000).
[19] E. Sörman, N. T. Son, W. M. Chen, O. Kordina, C. Hallin, and E. Janzén, Silicon vacancy related defect in 4H and 6H SiC, Phys. Rev. B **61**, 2613 (2000).
[20] N. Mizuochi, S. Yamasaki, H. Takizawa, N. Morishita, T. Ohshima, H. Itoh, and J. Isoya, Continuous-wave and pulsed EPR study of the negatively charged silicon vacancy with $S = 3/2$ and C3v symmetry in n-type 4H-SiC, Phys. Rev. B **66**, 235202 (2002).
[21] W. E. Carlos, N. Y. Garces, E. R. Glaser, and M. A. Fanton, Annealing of multivacancy defects in 4H−SiC, Phys. Rev. B **74**, 235201 (2006).
[22] S. B. Orlinski, J. Schmidt, E. N. Mokhov, and P. G. Baranov, Silicon and carbon vacancies in neutron-irradiated SiC: A high-field electron paramagnetic resonance study, Phys. Rev. B **67**, 125207 (2003).
[23] W. F. Koehl, B. B. Buckley, F. J. Heremans, G. Calusine, and D. D. Awschalom, Room temperature coherent control of defect spin qubits in silicon carbide, Nature (London) **479**, 84 (2011).
[24] V. A. Soltamov, A. A. Soltamova, P. G. Baranov, and I. I. Proskuryakov, Room Temperature Coherent Spin Alignment of Silicon Vacancies in 4H- and 6H-SiC, Phys. Rev. Lett. **108**, 226402 (2012).
[25] D. Riedel, F. Fuchs, H. Kraus, S. Vath, A. Sperlich, V. Dyakonov, A. A. Soltamova, P. G. Baranov, V. A. Ilyin, and G. V. Astakhov, Resonant Addressing and Manipulation of Silicon Vacancy Qubits in Silicon Carbide, Phys. Rev. Lett. **109**, 226402 (2012).
[26] F. Fuchs, V. A. Soltamov, S. Vath, P. G. Baranov, E. N. Mokhov, G. V. Astakhov, and V. Dyakonov, Silicon carbide light-emitting diode as a prospective room temperature source for single photons, Sci. Rep. **3**, 1637 (2013).
[27] S. Castelletto, B. C. Johnson, and A. Boretti, Quantum effects in silicon carbide hold promise for novel integrated devices and sensors, Adv. Opt. Mater. **1**, 609 (2013).
[28] A. L. Falk, B. B. Buckley, G. Calusine, W. F. Koehl, V. V. Dobrovitski, A. Politi, C. A. Zorman, P. X. L. Feng, and D. D. Awschalom, Polytype control of spin qubits in silicon carbide, Nat. Commun. **4**, 1819 (2013).
[29] S. Castelletto, B. C. Johnson, V. Ivady, N. Stavrias, T. Umeda, A. Gali, and T. Ohshima, A silicon carbide room-temperature single-photon source, Nat. Mater. **13**, 151 (2013).
[30] T. C. Hain, F. Fuchs, V. A. Soltamov, P. G. Baranov, G. V. Astakhov, T. Hertel, and V. Dyakonov, Excitation and recombination dynamics of vacancy-related spin centers in silicon carbide, J. Appl. Phys. **115**, 133508 (2014).
[31] S. Castelletto, B. C. Johnson, C. Zachreson, D. Beke, I. Balogh, T. Ohshima, I. Aharonovich, and A. Gali, Room temperature quantum emission from cubic silicon carbide nanoparticles, ACS Nano **8**, 7938 (2014).
[32] A. Muzha, F. Fuchs, N. V. Tarakina, D. Simin, M. Trupke, V. A. Soltamov, E. N. Mokhov, P. G. Baranov, V. Dyakonov, A. Krueger, and G. V. Astakhov, Room-temperature near-infrared silicon carbide nanocrystalline emitters based on optically aligned spin defects, Appl. Phys. Lett. **105**, 243112 (2014).
[33] H. Kraus, V. A. Soltamov, D. Riedel, S. Vath, F. Fuchs, A. Sperlich, P. G. Baranov, V. Dyakonov, and G. V. Astakhov, Room-temperature quantum microwave emitters based on spin defects in silicon carbide, Nat. Phys. **10**, 157 (2014).
[34] G. Calusine, A. Politi, and D. D. Awschalom, Silicon carbide photonic crystal cavities with integrated color centers, Appl. Phys. Lett. **105**, 011123 (2014).
[35] P. V. Klimov, A. L. Falk, B. B. Buckley, and D. D. Awschalom, Electrically Driven Spin Resonance in Silicon Carbide Color Centers, Phys. Rev. Lett. **112**, 087601 (2014).
[36] A. L. Falk, P. V. Klimov, B. B. Buckley, V. Ivady, I. A. Abrikosov, G. Calusine, W. F. Koehl, A. Gali, and D. D. Awschalom, Electrically and Mechanically Tunable Electron

Spins in Silicon Carbide Color Centers, Phys. Rev. Lett. **112**, 187601 (2014).

[37] H. Kraus, V. A. Soltamov, F. Fuchs, D. Simin, A. Sperlich, P. G. Baranov, G. V. Astakhov, and V. Dyakonov, Magnetic field and temperature sensing with atomic-scale spin defects in silicon carbide, Sci. Rep. **4**, 5303 (2014).

[38] L.-P. Yang, C. Burk, M. Widmann, S.-Y. Lee, J. Wrachtrup, and N. Zhao, Electron spin decoherence in silicon carbide nuclear spin bath, Phys. Rev. B **90**, 241203 (2014).

[39] V. A. Soltamov, B. V. Yavkin, D. O. Tolmachev, R. A. Babunts, A. G. Badalyan, V. Yu. Davydov, E. N. Mokhov, I. I. Proskuryakov, S. B. Orlinskii, and P. G. Baranov, Optically Addressable Silicon Vacancy-Related Spin Centers in Rhombic Silicon Carbide with High Breakdown Characteristics and ENDOR Evidence of their Structure, Phys. Rev. Lett. **115**, 247602 (2015).

[40] O. V. Zwier, D. O'Shea, A. R. Onur, and C. H. van der Wal, All-optical coherent population trapping with defect spin ensembles in silicon carbide, Sci. Rep. **5**, 10931 (2015).

[41] A. L. Falk, P. V. Klimov, V. Ivady, K. Szasz, D. J. Christle, W. F. Koehl, A. Gali, and D. D. Awschalom, Optical Polarization of Nuclear Spins in Silicon Carbide, Phys. Rev. Lett. **114**, 247603 (2015).

[42] S. G. Carter, Ö. O. Soykal, P. Dev, S. E. Economou, and E. R. Glaser, Spin coherence and echo modulation of the silicon vacancy in 4H-SiC at room temperature, Phys. Rev. B **92**, 161202 (2015).

[43] D. Simin, F. Fuchs, H. Kraus, A. Sperlich, P. G. Baranov, G. V. Astakhov, and V. Dyakonov, High-Precision Angle-Resolved Magnetometry with Uniaxial Quantum Centers in Silicon Carbide, Phys. Rev. Appl. **4**, 014009 (2015).

[44] S.-Y. Lee, M. Niethammer, and J. Wrachtrup, Vector magnetometry based on $S = 3/2$ electronic spins, Phys. Rev. B **92**, 115201 (2015).

[45] D. J. Christle, A. L. Falk, P. Andrich, P. V. Klimov, J. Ul Hassan, N. T. Son, E. Janzen, T. Ohshima, and D. D. Awschalom, Isolated electron spins in silicon carbide with millisecond coherence times, Nat. Mater. **14**, 160 (2015).

[46] M. Widmann, S.-Y. Lee, T. Rendler, N. T. Son, H. Fedder, S. Paik, L.-P. Yang, N. Zhao, S. Yang, I. Booker, A. Denisenko, M. Jamali, S. A. Momenzadeh, I. Gerhardt, T. Ohshima, A. Gali, E. Janzen, and J. Wrachtrup, Coherent control of single spins in silicon carbide at room temperature, Nat. Mater. **14**, 164 (2015).

[47] F. Fuchs, B. Stender, M. Trupke, D. Simin, J. Paum, V. Dyakonov, and G. V. Astakhov, Engineering near infrared single-photon emitters with optically active spins in ultrapure silicon carbide, Nat. Commun. **6**, 7578 (2015).

[48] A. Lohrmann, N. Iwamoto, Z. Bodrog, S. Castelletto, T. Ohshima, T. J. Karle, A. Gali, S. Prawer, J. C. McCallum, and B. C. Johnson, Single-photon emitting diode in silicon carbide, Nat. Commun. **6**, 7783 (2015).

[49] T. Wimbauer, B. K. Meyer, A. Hofstaetter, A. Scharmann, and H. Overhof, Negatively charged Si vacancy in 4H SiC: A comparison between theory and experiment, Phys. Rev. B **56**, 7384 (1997).

[50] H. J. Von Bardeleben, J. L. Cantin, E. Rauls, and U. Gerstmann, Identification and magneto-optical properties of the NV center in 4H−SiC, Phys. Rev. B **92**, 064104 (2015).

[51] S. A. Zargaleh, B. Eble, S. Hameau, J. L. Cantin, L. Legrand, M. Bernard, F. Margaillan, J. S. Lauret, J. F. Roch, H. J. Von Bardeleben, E. Rauls, U. Gerstmann, and F. Treussart, Evidence for near-infrared photoluminescence of nitrogen vacancy centers in 4H-SiC, Phys. Rev. B **94**, 060102 (2016).

[52] H. J. Von Bardeleben, J. L. Cantin, A. Csóré, A. Gali, E. Rauls, and U. Gerstmann, NV centers in 3*C*, 4*H*, and 6*H* silicon carbide: A variable platform for solid-state qubits and nanosensors, Phys. Rev. B **94**, 121202 (2016).

[53] A. Csóré, H. J. Von Bardeleben, J. L. Cantin, and A. Gali, Characterization and formation of NV centers in 3*C*, 4*H*, and 6*H* SiC: An *ab initio* study, Phys. Rev. B **96**, 085204 (2017).

[54] Yu. A. Vodakov, E. N. Mokhov, M. G. Ramm, and A. D. Roenkov, Epitaxial growth of silicon carbide layers by sublimation "sandwich method" (I) growth kinetics in vacuum, Krist. Tech. **14**, 729 (1979).

[55] V. G. Grachev, Correct expression for the generalized spin Hamiltonian for a noncubic paramagnetic center, Zh. Eksp. Teor. Phys. **92**, 1834 (1987) [Sov. Phys. JETP **65**, 7029 (1987)].

[56] Mt. Wagner, N. Q. Thinh, N. T. Son, W. M. Chen, E. Janzén, P. G. Baranov, E. N. Mokhov, C. Hallin, and J. L. Lindström, Ligand hyperfine interaction at the neutral silicon vacancy in 4H- and 6H-SiC, Phys. Rev. B **66**, 155214 (2002).

[57] T. Biktagirov, W. G. Schmidt, U. Gerstmann, B. Yavkin, S. Orlinskii, P. Baranov, V. Dyakonov, and V. Soltamov, Polytypism driven zero-field splitting of silicon vacancies in 6H-SiC, Phys. Rev. B **98**, 195204 (2018).

[58] See Supplemental Material at http://link.aps.org/supplemental/10.1103/PhysRevB.104.125205 for determination of the sign of the parameter D from the EPR spectra; the manifestation of the blind spot effect; and angular dependence ESE-detected EPR and ENDOR spectra of the V2 spin-3/2 centers in single 15R-SiC crystal.

[59] J.-M. Spaeth, J. R. Niklas, and R. H. Bartram, *Structural Analysis of Point Defects in Solids* (Springer-Verlag, Berlin, Heidelberg, 1992), Chap. 5, p. 152.

[60] P. G. Baranov, H.-J. von Bardeleben, F. Jelezko, and J. Wrachtrup, *Magnetic Resonance of Semiconductors and Their Nanostructures: Basic and Advanced Applications*, Springer Series in Materials Science, Vol. 253 (Springer-Verlag GmbH Austria, 2017), Chap. 6.

[61] W. B. Mims, in *Electron Paramagnetic Resonance*, edited by S. Geshwind (Plenum, New York, 1972), p. 344.

[62] C. Gemperle and A. Schweiger, Pulsed electron-nuclear double resonance methodology, Chem. Rev. **91**, 1481 (1991).

[63] G. Jeschke and A. Schweiger, Hyperfine-correlated electron nuclear double resonance spectroscopy, Chem. Phys. Lett. **246**, 431 (1995).

[64] G. V. Astakhov, D. Simin, V. Dyakonov, B. V. Yavkin, S. B. Orlinskii, I. I. Proskuryakov, A. N. Anisimov, V. A. Soltamov, and P. G. Baranov, Spin centers in SiC for quantum technologies, Appl. Magn. Reson. **47**, 793 (2016).

[65] C. J. Cochrane, J. Blacksberg, M. A. Anders, and P. M. Lenahan, Vectorized magnetometer for space applications using electrical readout of atomic scale defects in silicon carbide, Sci. Rep. **6**, 37077 (2016).

[66] A. van Duijn-Arnold, J. Mol, R. Verberk, J. Schmidt, E. N. Mokhov, and P. G. Baranov, Spatial distribution of the electronic wave function of the shallow boron acceptor in 4H- and 6H-SiC, Phys. Rev. B **60**, 15829 (1999).

[67] A. van Duijn-Arnold, R. Zondervan, J. Schmidt, P. G. Baranov, and E. N. Mokhov, Electronic structure of the N donor center in 4H-SiC and 6H-SiC, Phys. Rev. B **64**, 085206 (2001).

[68] N. T. Son, E. Janzén, J. Isoya, and S. Yamasaki, Hyperfine interaction of the nitrogen donor in 4H−SiC, Phys. Rev. B **70**, 193207 (2004).

[69] D. V. Savchenko, E. N. Kalabukhova, V. S. Kiselev, J. Hoentsch, and A. Poppl, Spin-coupling and hyperfine interaction of the nitrogen donors in 6H-SiC, Phys. Status Solidi B **246**, 1908 (2009).

[70] D. V. Savchenko, E. N. Kalabukhova, A. Poppl, and B. D. Shanina, Electronic structure of the nitrogen donors in 6H SiC as studied by pulsed ENDOR and TRIPLE ENDOR spectroscopy, Phys. Status Solidi B **249**, 2167 (2012).

[71] P. G. Baranov, B. Ya. Ber, O. N. Godisov, I. V. Il'in, A. N. Ionov, E. N. Mokhov, M. V. Muzafarova, A. K. Kaliteevskii, M. A. Kaliteevskii, and P. S. Kop'ev, Probing of the shallow donor and acceptor wave functions in silicon carbide and silicon through an EPR study of crystals with a modified isotopic composition, Phys. Solid State **47**, 2219 (2005).

[72] S. Greulich-Weber, M. Feege, J.-M. Spaeth, E. N. Kalabukhova, S. N. Lukin, and E. N. Mokhov, On the microscopic structures of shallow donors in 6H SiC: Studies with EPR and ENDOR, Solid State Commun. **93**, 393 (1995).

[73] N. T. Son, J. Isoya, T. Umeda, I. G. Ivanov, A. Henry, T. Ohshima, and E. Janzén, EPR and ENDOR studies of shallow donors in SiC, Appl. Magn. Reson. **39**, 49 (2010).

[74] J. R. Morton and K. F. Preston, Atomic parameters for paramagnetic resonance data, J. Magn. Res. **30**, 377 (1978).

[75] A. Abragam and B. Bleaney, *Electron Paramagnetic Resonance of Transition Ions* (Clarendon, Oxford, 1970), p. 702.

[76] A. Gali, M. Fyta, and E. Kaxiras, *Ab initio* supercell calculations on nitrogen-vacancy center in diamond: Electronic structure and hyperfine tensors, Phys. Rev. B **77**, 155206 (2008).

[77] V. Ivády, J. Davidsson, N. T. Son, T. Ohshima, I. Abrikosov, and A. Gali, Identification of Si-vacancy related room-temperature qubits in 4H silicon carbide, Phys. Rev. B **96**, 161114(R) (2017).

[78] J. Davidsson, V. Ivády, R. Armiento, T. Ohshima, N. T. Son, A. Gali, and I. A. Abrikosov, Identification of divacancy and silicon vacancy qubits in 6H-SiC, Appl. Phys. Lett. **114**, 112107 (2019).

[79] A. Csóré, N. T. Son, and A. Gali, Towards identification of silicon vacancy-related electron paramagnetic resonance centers in 4H-SiC, Phys. Rev. B **104**, 035207 (2021).